Effects of Ligand-Mimetic Peptides Arg-Gly-Asp-X (X = Phe, Trp, Ser) on αIIbβ3 Integrin Conformation and Oligomerization†

Roy R. Hantgan,*,‡ Christian Paumi,‡ Mattia Rocco,§ and John W. Weisel||

Department of Biochemistry, Wake Forest University School of Medicine, Medical Center Boulevard, Winston-Salem, North Carolina 27157, Gruppo di Biostrutture, Istituto Nazionale per la Ricerca sul Cancro (IST), Centro per le Biotecnologie Avanzate (CBA), Genova, Italy, and Department of Cell and Developmental Biology, University of Pennsylvania, Philadelphia, Pennsylvania 19104

Received April 2, 1999; Revised Manuscript Received July 19, 1999

ABSTRACT: The purpose of this investigation was to determine what structural changes convert "inert" αIIbβ3 integrins into "activated" high-affinity receptors for adhesive proteins. Light scattering, analytical ultracentrifugation, electron microscopy, and molecular modeling were used to probe the conformational states of the αIIbβ3 integrin. Isolated from human blood platelets in octyl glucoside, the αIIbβ3 complex behaved as an asymmetric 230 kDa macromolecule with a *z*-average translational diffusion coefficient of 2.9 F and a weight-average sedimentation coefficient of 7.7 S. Dynamic light scattering showed that ligand-mimetic peptides (RGDX, X = F, W, S) caused prompt, concentration-dependent increases in the Stokes radius (R_s) of the αIIbβ3 complex, whereas control peptides of reversed sequence (XDGR, X = F, W, S) had no significant effect. Sedimentation velocity data coupled with time-derivative analyses showed that RGDX peptides shifted the distribution of αIIbβ3 sedimenting species toward smaller *s* values. Sedimentation equilibrium measurements indicated that a slower increase in the αIIbβ3 molecular weight distribution took place in the presence of RGDX ligand-mimetics. Electron microscopy showed a split of αIIbβ3's globular domain into two distinct nodules in the presence of RGDX peptides; oligomers joined through their stalk regions were seen frequently. These observations suggest that receptor occupancy by ligand-mimetic RGDX peptides is tightly coupled to relatively large changes in the structure of the αIIbβ3 complex. αIIbβ3 bead models were developed to describe quantitatively the ligand-induced transition from a "closed" to an "open" integrin conformation and the limited oligomerization that follows. This provides a new mechanistic framework for understanding integrin activation and the formation of signaling clusters on the surface of stimulated platelets.

Integrins are the major class of transmembrane receptors responsible for cell−cell and cell−matrix interactions (*1*−*3*), ranging from embryonic development, cell differentiation, and migration to programmed cell death (*4, 5*). Integrins also contribute to pathophysiological processes that involve blood clotting and inflammation as well as tumor growth and metastasis (*6, 7*). Despite major advances in cell and molecular biology in the past decade, many questions remain concerning the relationship between integrin structure and function (*1, 8*). This work examines the conformational states of one integrin, the αIIbβ3 complex, using an integrated biophysical, electron microscope and molecular modeling approach.

The 22 known members of the integrin superfamily are all heterodimers, formed by the noncovalent association of α and β subunits that range in size from 90 to 200 kDa (*9*). Features common to most integrin subunits include a large extracellular domain, a single membrane-spanning region, and a small carboxy-terminal intracellular domain (*10*−*12*). While only limited high-resolution data are available (*13*−*15*), several lines of evidence demonstrate that a conserved feature of integrin quaternary structure is the divalent metal ion-dependent association of the extracellular regions of the α and β subunits to form a ligand-recognition surface (*16*−*19*).

Affinity modulation is a hallmark of several members of the integrin superfamily, including the αIIbβ3 integrin (*20*−*22*). Present at remarkably high density on the surface of circulating human blood platelets, the 226 kDa αIIbβ3 complex can serve as a high-affinity adhesive protein receptor only after platelets have been activated by a stimulus such as thrombin or ADP (*8, 23*). These stimuli trigger myriad cytoplasmic pathways that involve calcium fluxes, phospholipid metabolism, GTP-binding proteins, and protein kinases, as well as cytoskeleton proteins (*2, 24*).

Parallel changes in the αIIbβ3 complex occur in a process termed "inside-out" signaling that enables these newly "activated" receptors to bind adhesive proteins such as fibrinogen with greatly increased affinity (*2, 9, 23*). Evidence for a linkage between platelet activation and changes in

† Support provided by Grant MCB-9728122 from the National Science Foundation (to R.R.H.), Grant BI04-CT96-0662 from the European Community (to M.R.), and Grant HL30954 from the National Institutes of Health (to J.W.W.).

* To whom correspondence should be addressed. Phone: (336) 716-4675. Fax: (336) 716-7671. E-mail: rhantgan@wfubmc.edu.

‡ Wake Forest University School of Medicine.

§ Centro per le Biotecnologie Avanzate.

|| University of Pennsylvania.

10.1021/bi9907680 CCC: $18.00
Published on Web 10/14/1999

αIIbβ3 conformation comes from fluorescence energy transfer measurements that demonstrated changes in the intersubunit distances of the membrane-bound αIIb and β3 polypeptides during the activation process (*25*).

Receptor occupancy itself initiates a cascade of intracellular events termed "outside-in signaling" that involves integrin structural alterations, receptor clustering, and stabilization of the initially reversible ligand binding (*1, 2, 6*). Evidence that ligand binding is coupled to conformational changes in the platelet-bound αIIbβ3 complex comes from the demonstration of neoantigenic sites on the receptor following cellular exposure to ADP and fibrinogen or to synthetic peptides that contain an Arg-Gly-Asp (RGD) integrin-targeting sequence (*26*).

Ligand-induced conformational changes leading to a functional receptor have also been described for the purified αIIbβ3 complex (*21, 27*). For example, prolonged incubation with either RGDS[1] or a synthetic peptide corresponding to the carboxy-terminal integrin binding site on fibrinogen (LGGAKQAGDV) has been shown to increase the Stokes radius and decrease the sedimentation coefficient of the αIIbβ3 complex (*28*). NMR studies have indicated that GRGDSP can also induce conformational changes in the αIIbβ3 complex (*29*). However, these experiments were performed in the presence of concentrations of sodium dodecyl sulfate that may have perturbed the native structure of the isolated integrin. Evidence for ligand-coupled integrin clustering has also been obtained with αIIbβ3 reconstituted into a lipid environment. Interestingly, the multivalent ligand fibrinogen caused receptor self-association, but monovalent ligand-mimetic peptides did not (*30*).

Given the recent interest in understanding integrin affinity modulation and signaling in structural terms (*31*−*33*), we initiated a study of the effects of a series of ligand-mimetic peptides of sequence RGDX on αIIbβ3 conformation and oligomerization. The solution structure of the αIIbβ3 complex, isolated in the nondenaturing detergent octyl glucoside, was characterized by a combined hydrodynamic and thermodynamic approach. This involved classical and dynamic light scattering (*34*) as well as sedimentation velocity and equilibrium measurements (*35*), each performed in the presence/absence of a set of low molecular weight ligands. Complementary structural insights were obtained by transmission electron microscopy (*17*). Results will be discussed in terms of a new series of domain models (*36*) for the initial and ligand-bound αIIbβ3 complex.

EXPERIMENTAL PROCEDURES

Purification of the αIIbβ3 Complex. The platelet integrin receptor αIIbβ3 was isolated from human blood platelets (American Red Cross, Triad Blood Center, Winston-Salem, NC) by methods previously described in detail (*34*), with the following modifications. Samples enriched in αIIbβ3 by cell fractionation and lentil lectin chromatography (Pharmacia, Piscataway, NJ) were eluted from a 0.9 × 85 cm column of Ultrogel 34 (LKB, Bromma, Sweden) at 4 °C in a pH 7.4 buffer containing 0.13 M NaCl, 0.01 M HEPES, 0.002 M $CaCl_2$, 3×10^{-8} M basic trypsin inhibitor (aprotinin, Sigma), 10^{-6} M leupeptin, and 0.03 M *n*-octyl β-D-glucopyranoside (octyl glucoside, OG, Sigma). Peak fractions were then concentrated in an Amicon pressure concentrator with a PLHK cellulose membrane, 100 000 Da retention limit (chosen for its low protein binding). When required, rapid buffer exchange or peptide removal was accomplished by sedimenting αIIbβ3 samples (0.1 mL) through 1 mL columns of G-25 Sephadex (Pharmacia) at 1000*g* for 2 min. Samples characterized by SDS−PAGE followed by staining with Coomassie Brilliant Blue R-250 exhibited polypeptides with electrophoretic mobilities on nonreduced and reduced samples characteristic of the α and β subunits of the platelet integrin receptor (*34, 37*). αIIbβ3 concentrations were determined by ultraviolet absorbance measurements (LKB Ultrospec) using an extinction coefficient at 280 m of 1.21 mL mg^{-1} cm^{-1}, as previously described (*34, 38*).

Ligand-Mimetic Peptides. The following peptides were synthesized by the Protein Analysis Core Laboratory of the Comprehensive Cancer Center of Wake Forest University (Winston-Salem, NC): L-arginyl-L-aspartyl-glycyl-L-phenylalanine (RGDF), L-arginyl-L-aspartyl-glycyl-L-tryptophan (RGDW), L-arginyl-L-aspartyl-glycyl-L-serine (RGDS), L-phenylalanyl-L-aspartyl-glycyl-L-arginine (FDGR), L-tryptophanyl-L-aspartyl-glycyl-L-arginine (WDGR), and L-seryl-L-aspartyl-glycyl-L-arginine (SDGR). Each synthesis was carried out on an automated peptide synthesizer (model 430A, Applied Biosystems, Inc., Foster City, CA) using previously described protocols (*39*). Each peptide was characterized by high-performance liquid chromatography and shown to have the correct amino acid sequence using an Applied Biosystems 475 automated peptide sequencer (*39*). Peptide concentrations were determined by quantitative amino acid composition analyses (*39*) of samples of stock solutions (that were stored for up to 6 months at −70 °C).

Static and Dynamic Light Scattering: Instrumentation and Data Analyses. Measurements of the molecular weight and translational diffusion coefficient of the αIIbβ3 complex were performed with a Brookhaven Instruments BI-2030 AT correlator, operated in conjunction with a BI-200 SM light scattering goniometer/photon counting detector and a Spectra Physics 127 He−Ne laser (35 mW, equipped with a vertical polarization rotator) as previously described (*34*), with the following modifications. Light was collected at a right angle from samples of αIIbβ3 or buffered octyl glucoside contained in specially formulated Ultra-Micro cuvettes with three windows and a filling volume of 120 μL (Hellma Cells, Inc., Forest Hills, NY). Each cuvette was contained in a thermostated (25.0 °C) refractive-index-matching bath (*34*).

For molecular weight determinations, sample scattering intensities were corrected for solvent scattering and expressed relative to that of a benzene standard (*34*). This information coupled with measurements of protein concentration by UV absorbance and a refractive index increment (d*n*/d*c*) of 0.243 cm^3 g^{-1} (*34*) was used to calculate the weight-average molecular weight of αIIbβ3 samples using Rayleigh−Gans−Debye theory (*40*). For translational diffusion coefficient determinations, each intensity-normalized photon count au-

[1] Abbreviations: OG, *n*-octyl β-D-glucopyranoside (octyl glucoside); RGDF, L-arginyl-L-aspartyl-glycyl-L-phenylalanine; RGDW, L-arginyl-L-aspartyl-glycyl-L-tryptophan; RGDS, L-arginyl-L-aspartyl-glycyl-L-serine; RGDX, L-arginyl-L-aspartyl-glycyl-L-phenylalanine, L-arginyl-L-aspartyl-glycyl-L-tryptophan, L-arginyl-L-aspartyl-glycyl-L-serine; FDGR, L-phenylalanyl-L-aspartyl-glycyl-L-arginine; WDGR, L-tryptophanyl-L-aspartyl-glycyl-L-arginine; SDGR, L-seryl-L-aspartyl-glycyl-L-arginine; BEADS, beads modeling system; PROMOLP, protein molecular parameters; GRUMB, graphical utilities for modeling with beads.

tocorrelation function obtained for the αIIbβ3 complex was corrected for the contributions of octyl glucoside micelles and then analyzed by the method of cumulants, as previously described (*34*).

Analytical Ultracentrifugation: Instrumentation and Data Analyses. Sedimentation velocity and equilibrium measurements were performed in a Beckman Optima XL-A analytical ultracentrifuge (Beckman Instruments, Palo Alto, CA) equipped with absorbance optics and an An60 Ti rotor. Sedimentation velocity data for the αIIbβ3 complex (alone and in the presence of ligand-mimetic or control peptides) were obtained in double-sector cells at 20 °C at a rotor speed of 35 000 rpm. Data were collected at 280 or 250 nm (with buffered octyl glucoside and, in selected cases, peptides in the reference sector) using a radial step size of 0.003 or 0.005 cm during the course of 3−5 h runs.

These data were analyzed using time-derivative software (DCDT) provided by Dr. Walter Stafford (Boston Biomedical Research Institute) to obtain the distribution of sedimenting species, g(s*) (*41*). This process was repeated with four to six sets of closely spaced sequential scans obtained during the course of each sedimentation versus time profile, taking care to meet the criterion that the time interval between the first and last scan in each set not exceed the limit required by the DCDT algorithm (*41*). The weight-average sedimentation coefficient was obtained from each set by integrating the $g(s^*)$ profile; the resultant s^*_w values were plotted versus $1/t$ and extrapolated to $1/t = 0$ to obtain a value for s_w corrected for the contributions of diffusion (*41*). In addition, the Claverie simulation (*42*, *43*) utility of SVEDBERG software (*44*) (purchased from Dr. John Philo) was used to generate sedimentation velocity data sets, using experimentally determined sedimentation and diffusion coefficients as input parameters. These simulated data were then analyzed with DCDT software to yield computed $g(s^*)$ profiles for comparison to experiment.

Sedimentation equilibrium data were collected from αIIbβ3 samples (alone and in the presence of ligand-mimetic or control peptides) contained in double-sector cells with buffered octyl glucoside (and peptides, as required) in the reference sector. Data were collected at 280 nm at rotor speeds of 5000, 6000, and 8000 rpm at 20 °C. The rotor was run at each speed for 18 h, and then scans were obtained at 20, 22, and 24 h. Scans were performed with a radial step size of 0.001 cm, and three averages were obtained in the continuous scan mode. Sequential scans at each rotor speed were compared with MATCH software (*45*) to select those that met equilibrium conditions. Truncated datasets (radial distance beyond the sample meniscus; maximum absorbance 1.5) were obtained from these files with REEDIT software (*45*).

These data, absorbance vs radial distance, were analyzed by nonlinear regression with NONLIN to obtain the weight-average buoyant molecular weight σ [and thus M_w (*45*)] for the αIIbβ3 complex alone and in the presence of ligand-mimetic (or control) peptides. A value of $\upsilon = 0.718$ cm^3 g^{-1} was calculated for αIIbβ3 from the amino acid and carbohydrate compositions of the α and β polypeptides with correction for detergent binding (*36*). A solvent density = 1.008 g/cm^3 was determined for buffered octyl glucoside using a DA-130 M precision densitometer thermostated at 20 °C. NONLIN was used to perform global fits using input data at a range of macromolecular concentrations and rotor speeds to obtain a best fit value of M_w. MATCH, REEDIT, and NONLIN have been provided by Dr. Emory Braswell and the staff at the National Analytical Ultracentrifugation Facility, Storrs, CT.

Rotary-Shadowed Specimens for Electron Microscopy. Rotary-shadowed samples were prepared by spraying a dilute solution (final concentration of about 20 μg/mL) of molecules in a volatile buffer [0.05 M ammonium formate at pH 7.4, 30 mM octyl glucoside, and 70% (v/v) glycerol] onto freshly cleaved mica and shadowing with tungsten in a vacuum evaporator (Denton Vacuum Co., Cherry Hill, NJ) (*46*−*48*). These samples were examined in a Philips 400 electron microscope (FEI Co., Hillsboro, OR), operating at 80 kV and a magnification of 60 000×. Counts of molecules with different conformations or different amounts of oligomers were made from prints of the micrographs, using images from many different areas of several different preparations to get a random sample.

Selected light scattering measurements were also performed with αIIbβ3 samples quickly equilibrated in a volatile buffer similar to that used for electron microscopy, i.e., 0.05 M ammonium formate at pH 7.4, 30 mM octyl glucoside, and 30% (v/v) glycerol. The glycerol concentration was limited to 30%, as experiments with 20 nm diameter latex spheres (Duke Scientific Co.) demonstrated that this concentration reduced the scattering intensity by ∼40% and decreased the apparent diffusion coefficient by a factor of 3, effects due to changes in solvent refractive index and viscosity, respectively (*49*).

Bead Modeling. Bead models of the αIIbβ3 complex were constructed, visualized, and analyzed using the BEAMS (beads modeling system) set of computer programs developed by Rocco et al. (*36*, *50*). In short, the αIIb and β3 polypeptide chains of the αIIbβ3 complex were each represented as an ensemble of interconnected spheres. The size and sequence boundaries of each 5−10 kDa sphere were defined by biochemical, immunological, or electron microscope criteria (*36*), utilizing the ancillary program PROMOLP[2] (protein molecular parameters). On the basis of recent reports (*51*, *52*), the bead volume due to bound water was reduced ∼18% compared to our earlier model (*36*); as a result, 44 slightly smaller beads were used here to model the αIIbβ3 complex. Table 2 (see Appendix) reports the bead sequence assignments and molecular parameters.

These modifications were aided by the ancillary program GRUMB (graphical utilities for modeling with beads) (*50*), which also enables the visualization of the bead models through the public domain software RasMol (*53*). The BEAMS routine SUPC, which employs the hydrodynamic theory for multisubunit particles (*50*, *54*) to calculate solution parameters of arrays of up to 1000 nonoverlapping beads, was then used to calculate (at standard conditions: water at 20 °C) the translational diffusion coefficient, D_t, the Stokes radius, R_s, and the sedimentation coefficient, s, for the models. These calculations utilized molecular weights of 130 592, 95 396 (PROMOLP values), and 6000 (*34*) and υ

[2] PROMOLP (protein molecular parameters): Windows-based software for the computation of physicochemical parameters of proteins from primary structure data (M. Rocco, M. Martinis, C. Ruggerio, and M. Molina, personal communication).

values of 0.716, 0.711 (PROMOLP values), and 0.86 (*55*) $cm^3\ g^{-1}$ for the αIIb and β3 subunits and for the OG micelle, respectively. Coordinates and other parameters of the bead models as well as the RasMol script files are available in the electronic supplement to this paper (see Supporting Inforation).

RESULTS

Characterization of the αIIbβ3 Complex. (A) Molecular Weight. Light scattering intensity measurements were performed on samples of the αIIbβ3 complex isolated by size-exclusion chromatography in octyl glucoside. Analysis of these data by Rayleigh−Gans−Debye theory (*40*) yielded a weight-average molecular weight of $(2.07 \pm 0.16) \times 10^5$ ($n = 17$; 0.28−1.03 mg/mL). This result is in close agreement with our earlier experimental observations (*34*) and the value of 2.26×10^5 calculated for the polypeptide chains from primary structural data (*56*).

Molecular weight determinations were also performed by the technique of sedimentation equilibrium, carried out as a function of αIIbβ3 concentration (0.03−0.79 mg/mL) and rotor speed (5000, 6000, and 8000 rpm). Analyses of the individual datasets yielded molecular weights that exhibited no significant dependence on either protein concentration or rotor speed, consistent with a single ideal-species model (*45*). Representative data are shown in Figure 1A. Therefore, 15 datasets were analyzed globally (*45*) to yield a weight-average molecular weight of $(2.29 \pm 0.10) \times 10^5$ for the αIIbβ3 complex. We note that sedimentation equilibrium (unlike static light scattering) yields a molecular weight that includes contributions from bound detergent (*57*), which in this case increases the calculated molecular weight to 2.32×10^5 for the αIIbβ3 complex isolated in octyl glucoside (*34*).

(B) Hydrodynamic Properties. Dynamic light scattering data yielded a translational diffusion coefficient (extrapolated to zero concentration and corrected to water at 20 °C) of $D^0_{20,w} = 2.92 \pm 0.16$ F ($n = 17$; 0.28−1.03 mg/mL; F = Ficks, $1F = 10^{-7}\ cm^2\ s^{-1}$) for the αIIbβ3 complex (in octyl glucoside) that stands in excellent agreement with our previous results (*34*, *36*).

Sedimentation velocity measurements performed on the αIIbβ3 complex were each analyzed by the time-derivative method (*41*) to obtain profiles of the distribution of sedimenting species as a function of time. Representative plots of $g(s^*)$ vs s^* are shown in Figure 1B for three sequential time windows during the course of a single sedimentation velocity experiment carried out at 35 000 rpm. Note that while the peak position was essentially invariant at 8.4 S, the distribution became sharper with increasing sedimentation time, as expected for a single, noninteracting species (*41*).

Weight-average sedimentation coefficients, s_w, obtained by integrating these $g(s^*)$ profiles, were somewhat dependent on both the limits of integration and sedimentation time. Therefore, the effects of the octyl glucoside micelles [molecular weight ~6000; calculated sedimentation coefficient <1 S (*34*)] were minimized by setting 1 S as the lower limit of integration. Time dependence was considered by plotting s^*_w vs $1/t$ and extrapolating to $1/t = 0$ to obtain a diffusion-corrected s_w parameter (*41*). The resultant s_w values were extrapolated to zero αIIbβ3 concentration. Analysis of the complete dataset ($n = 9$; 0.07−0.76 mg/mL), including corrections for concentration dependence, solvent density, and viscosity (*58*), yielded $s^0_{20,w} = 7.66 \pm 0.39$ S. A similar analysis of the peak sedimentation coefficient data yielded an extrapolated value of 8.4 ± 0.2 S.

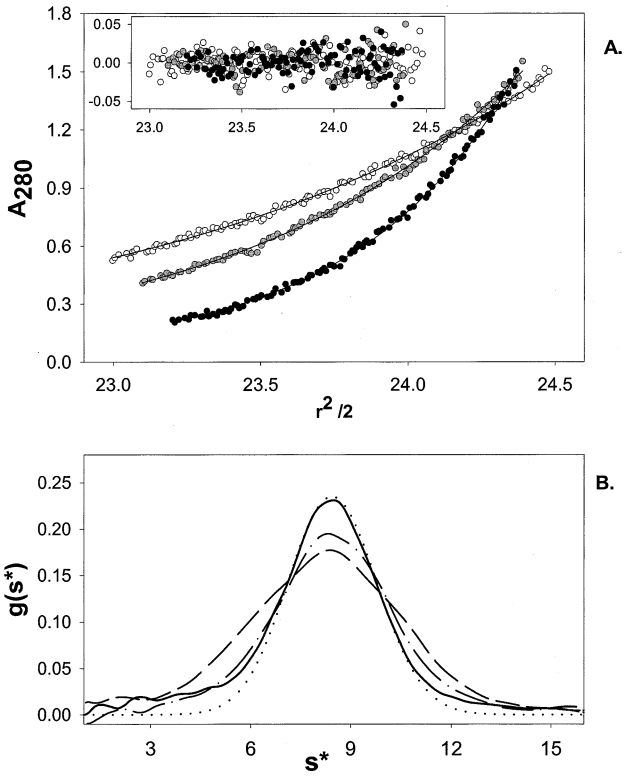

FIGURE 1: Characterization of the αIIbβ3 complex by analytical ultracentrifugation. Upper panel: Sedimentation equilibrium profiles for αIIbβ3 (0.74 mg/mL) in buffered octyl glucoside, expressed as absorbance at 280 nm vs square of the radial distance. Data presented were obtained at three different rotor speeds, following a 22 h equilibration period at each speed: open circles (5000 rpm), gray circles (6000 rpm), and black circles (8000 rpm). Solid lines were obtained by fitting the complete dataset (15 files) to a single ideal species model (using NONLIN); this procedure yielded $M_w = 229 \pm 10$ K. Deviations between the calculated and experimental points are shown in the insert. Lower panel: Sedimentation velocity profiles for αIIbβ3 (0.72 mg/mL) in buffered octyl glucoside, expressed as the apparent sedimentation coefficient distribution function, $g(s^*)$ vs s^*, the apparent sedimentation coefficient (i.e., not corrected for diffusion). Lines depict profiles obtained by time-derivative analyses (DCDT) of data obtained following sedimentation at 35 000 rpm (20 °C) for the following times: 2717 s (dashed), 4158 s (dash-dotted), and 5997 s (solid). Note that the peak is nearly invariant at 8.4 S (corrected to water at 20 °C). Integration of these profiles yielded a set of weight-average sedimentation coefficients that were extrapolated to $1/t = 0$ to obtain $s_{20,w} = 8.24 \pm 0.11$ S for this experiment. The dotted line was obtained by processing data from a Claverie simulation with the DCDT algorithm and corresponds to 8.4 S and 2.9 F.

Given these indications of sample heterogeneity, efforts were made to compare the experimentally determined $g(s^*)$ profile to that expected for a single sedimenting species. Thus a Claverie simulation (*42*−*44*) was performed using the experimentally determined sedimentation and diffusion coefficients of 8.4 S and 2.9 F, respectively. The resultant simulated data were analyzed by the DCDT algorithm to obtain a computed $g(s^*)$ profile, which is shown as a dashed line in Figure 1B. A very similar $g(s^*)$ profile was obtained using hydrodynamic parameters computed from a model of the αIIbβ3 complex (described in a later section). While the

Table 1: Biophysical Characterization of the αIIbβ3 Integrin

parameter	technique	result
molecular weight	static light scattering	207 ± 16 K[a]
molecular weight	sedimentation equilibrium	229 ± 10 K[b]
molecular weight	hydrodynamics (*s* and *D*)	231 ± 14 K[b]
translational diffusion coeff	dynamic light scattering	2.92 ± 0.16 F
sedimentation coeff (weight average)	sedimentation velocity	7.66 ± 0.39 S
sedimentation coeff (peak)	sedimentation velocity	8.40 ± 0.20 S

[a] Polypeptide chain. [b] Polypeptide chain plus bound detergent.

calculated line corresponds quite closely to the main peak of the experimental profile, this analysis does reveal the presence of small quantities of species running at <6 S and >12 S.

Summary of the Biophysical Properties of the αIIbβ3 Complex. Table 1 summarizes our biophysical characterization of the αIIbβ3 complex. We note that the molecular weight values determined by three independent methods, namely, static light scattering, sedimentation equilibrium, and hydrodynamics [calculated from $s^0_{20,w}$ and $D^0_{20,w}$ using the Svedberg equation (*58*)], are in excellent agreement with the value of 232 K derived from amino acid and carbohydrate composition data (*56*). Both the sedimentation and diffusion coefficients are consistent with an asymmetric shape for the αIIbβ3 complex, since a spherical macromolecule with bound water and detergent would exhibit a translational diffusion coefficient of 4.2 F and a sedimentation coefficient of 11 S (*58*), values nearly 50% greater than our experimental parameters. However, the experimentally determined hydrodynamic values are in close agreement with the properties of a domain model of the αIIbβ3 complex that we reported earlier (*34, 36*). This characterization of the native state of the αIIbβ3 complex will form the basis for judging the effects of receptor occupancy by ligand-mimetic peptides, described next.

Effects of Ligand-Mimetic Peptides on αIIbβ3 Physical Properties. (A) Biological Activity. Prior to their use in biophysical measurements, the biological activity of each peptide was measured in a platelet aggregation assay, and the data were analyzed to determine the peptide concentration required to reduce the initial rate of aggregation to 50% of its control value, denoted the IC_{50} (*39*). The active peptides (i.e., those with sequence RGDX) exhibited the following IC_{50} values: RGDF, 43 ± 10 μM; RGDW, 20 ± 3 μM; RGDS, 200 ± 25 μM. Control peptides (i.e., those with reversed sequence XDGR) had no significant effect on platelet aggregation at concentrations up to 750 μM.

(B) Stokes Radius. Dynamic light scattering measurements were performed on samples of αIIbβ3 following addition of ligand-mimetics of sequence RGDX to achieve peptide concentrations in the range 0.05−0.6 mM. Consider first RGDF, where an increase in the Stokes radius ($R_s = kT/D_{trans}$) was observed within 10 min of peptide addition. Data collected over a subsequent 3−4 h interval indicated that these changes were stable, leading to a 14 ± 4% ($n = 6$) increase in R_s in the presence of RGDF at concentrations in excess of 0.15 mM. In contrast, addition of FDGR caused only a 3 ± 1% (n=2) increase in R_s. These changes in the Stokes radius exhibited a hyperbolic dependence on RGDF concentration and appeared to approach saturation at the highest concentrations examined (Figure 2A). In contrast, only small changes in molecular weight (determined from the scattering intensity) were observed in the presence of either RGDF or control peptide FDGR (Figure 2B).

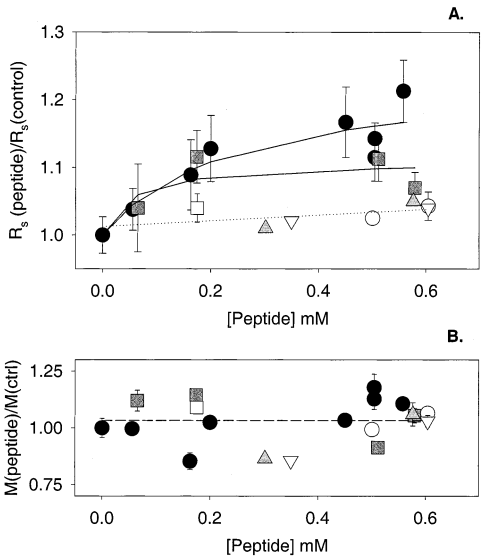

FIGURE 2: Effects of ligand-mimetic peptides on αIIbβ3 solution conformation determined by dynamic and static light scattering. Upper panel: Fractional change in the αIIbβ3 Stokes radius as a function of peptide concentration for active RGDX peptides (filled symbols) and control XDGR peptides (open symbols); X = F (circles), W (squares), and S (triangles). Data were obtained by dynamic light scattering measurements of the right angle intensity autocorrelation function of αIIbβ3 ± peptide, analyzed by the method of cumulants, following correction for solvent contributions. Error bars depict the standard deviation of replicate measurements (n = 7−10) performed on each sample. Note the approximate hyperbolic increase in R_s observed with RGDF and RGDW and the linear concentration dependence observed with RGDS and all three control peptides. Lower panel: Fractional change in αIIbβ3 molecular weight in the presence of active RGDX and control XDGR peptides (symbols as in upper panel). Data were obtained by static light scattering measurements of samples of αIIbβ3 ± peptide. The dashed line denotes the average M(peptide)/M(control) = 1.03 ± 0.10 for the entire dataset.

RGDW also yielded a specific, concentration-dependent increase in R_s for the αIIbβ3 complex. The maximum change determined with RGDW (10 ± 3%; $n = 3$, at >0.15 mM peptide) was comparble to that found with RGDF, and it exceeded the 4% increase in R_s measured with control peptide WDGR (Figure 2A). Only small changes in molecular weight were observed in the presence of either RGDW or WDGR (Figure 2B).

RGDS was found to be the least effective modulator of αIIbβ3 conformation in that a maximum 5% increase in R_s was observed at 0.58 mM peptide, compared to a 3% increase with SDGR (Figure 2A). However, both the Stokes radius and the molecular weight distribution exhibited small, time-dependent increases over a period of 4 h in the presence of RGDS (data not shown).

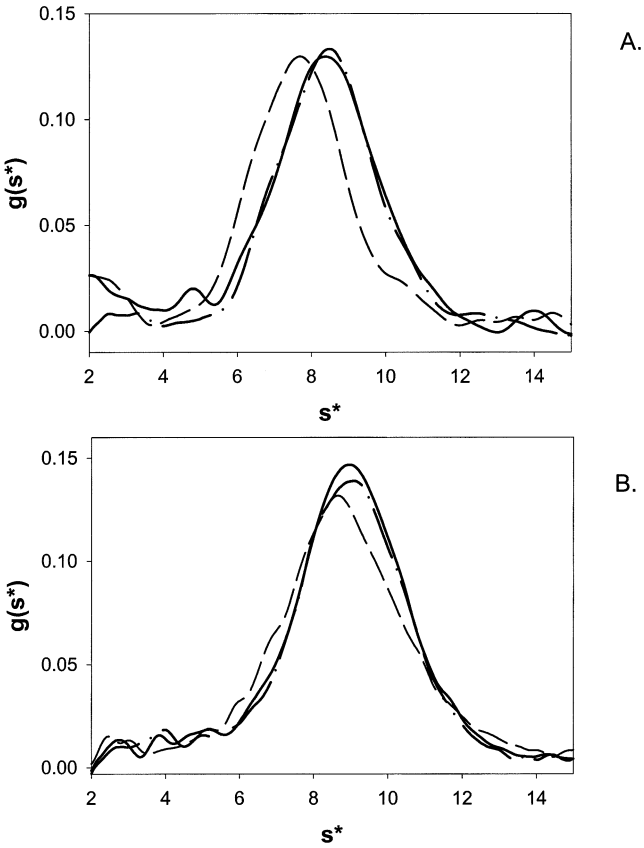

FIGURE 3: Effects of ligand-mimetic peptides on αIIbβ3 solution conformation determined by sedimentation velocity measurements. Upper panel: Sedimentation coefficient distribution functions, $g(s^*)$ vs s^*, obtained with αIIbβ3 alone (solid line) and in the presence of the ligand-mimetic peptide RGDF (dashed line) and the control peptide FDGR (dash-dotted line). Data were obtained by time-derivative analyses of data collected from samples of αIIbβ3 ± peptide (0.3 mM) during sedimentation at 35 000 rpm for ~6000 s. Note the shift in peak position from 8.4 S (αIIbβ3 alone) to 7.7 S in the presence of RGDF; with FDGR, the peak was 8.5 S (corrected to water at 20 °C). Lower panel: $g(s^*)$ vs s^* profiles for αIIbβ3 alone (solid line; peak at 9.0 S), in the presence of 0.6 mM RGDS (dashed line; peak at 8.7 S), and in the presence of SDGR (dash-dotted line; peak at 9.1 S).

Taken together, these dynamic and static light scattering measurements provide evidence for prompt ligand-induced conformational changes in the αIIbβ3 complex, with minimal changes in its molecular weight distribution. The magnitude of these structural changes, as described by the ratio of R_s in the presence of RGDX peptide to its corresponding control value, provided evidence that a hydrophobic residue may be preferred in the fourth position. These issues were investigated further by a series of analytical ultracentrifugation experiments designed to detect changes in either the conformation and/or oligomerization state of the αIIbβ3 complex.

(C) Sedimentation Coefficient. Sedimentation velocity data obtained with the αIIbβ3 complex in the presence/absence of ligand-mimetic or control peptides were analyzed by the time-derivative method to extract the distribution of sedimenting species (*41*). Representative data are shown in Figure 3A as a plot of the apparent sedimentation coefficient distribution, $g(s^*)$, vs s^*, for αIIbβ3 alone and in the presence of RGDF (0.28 mM) and FDGR (0.31 mM). (All sedimentation coefficients have been corrected to water at 20 °C.) The $g(s^*)$ profile for αIIbβ3 in the absence of ligand exhibited a peak at 8.4 S. A shift toward lower s values was observed in the presence of RGDF, with the peak in the $g(s^*)$ distribution now at 7.7 S. Control peptide FGDR had minimal impact on this function, with a peak value of 8.5 S. Additional sedimentation velocity experiments demonstrated similar shifts in the $g(s^*)$ profile at RGDF concentrations ranging from 0.05 to 0.54 mM. In fact, the ratio of s_{peak} in the presence/absence of RGDF was 0.936 ± 0.010 ($n = 5$), whereas this parameter equaled 1.06 ± 0.06 ($n = 2$) for control peptide FDGR.

As shown in Figure 3B, a peak shift of similar direction but smaller magnitude was also observed with 0.6 mM RGDS (from 9.0 to 8.7 S) but not SDGR (9.1 S). Here some oligomers were probably present in the αIIbβ3 preparation used for this experiment, as evidenced by its higher initial s value and unresolved shoulders between 10 and 12 S. However, the quantity of oligomeric species appeared to increase even further following the addition of RGDS. This point was explored further by Claverie/DCDT simulations (*42*−*44*), which revealed that, in the presence of RGDS, the peak was not only shifted toward lower s values but also contained additional material sedimenting at >10 S. These indications of RGDS-induced receptor oligomerization are consistent with light scattering (previous section) and sedimentation equilibrium data (subsequent section) we have obtained with this ligand-mimetic peptide.

Similar experiments were performed with RGDW; however, its increased UV absorbance required limiting the peptide concentration to 0.21 mM and collecting data at 250 nm (a trough in the absorbance spectrum). Despite these precautions, a noisier signal was still obtained. Here a minor peak shift was observed, from 8.0 to 7.9 S in the presence of RGDW, whereas a peak at 8.0 S was obtained with control peptide WDGR (data not shown).

(D) Molecular Weight Distribution. Analytical ultracentrifugation experiments (i.e., sedimentation equilibrium measurements) were performed to determine the extent to which RGDX peptides could alter the molecular weight distribution of the αIIbβ3 complex. Representative data are shown in Figure 4. Global analyses of sedimentation equilibrium data obtained in the presence of RGDF (0.3−0.6 mM) yielded $M_w = 254 \pm 14$ K ($n = 3$), while $M_w = 236 \pm 11$ K ($n = 3$) resulted in the presence of FDGR (0.3−0.6 mM). Similar analyses yielded a comparable weight-average molecular weight of 229 ± 10 K ($n = 7$) for the αIIbβ3 complex alone. These analyses indicate the presence of a small quantity of higher molecular weight material in the presence of RGDF.

The effects of RGDS were also examined by sedimentation equilibrium runs at a single rotor speed (8000 rpm), in an effort to minimize the time-dependent increases in molecular weight observed with this peptide by static light scattering. These data yielded comparable M_w values for the αIIbβ3 complex alone and in the presence of 0.58 mM SDGR (191 and 196 K, respectively). However, a higher M_w was obtained with 0.58 mM RGDS (260 K), indicative of increased oligomerization. In contrast, the presence of RGDW (0.08 mM) had no significant influence as $M_w = 222$ K resulted. Higher concentrations were not examined, due to problems associated with the strong UV absorbance of this tryptophan-containing peptide.

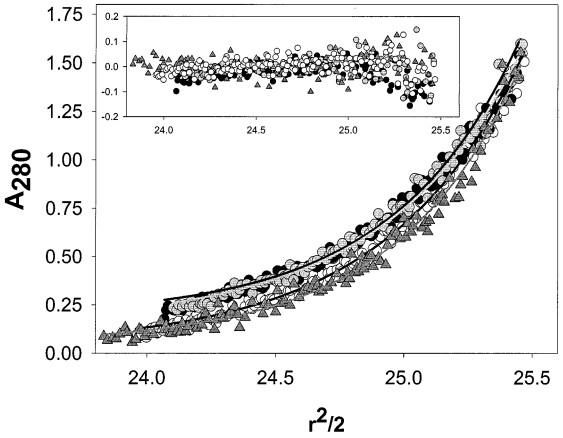

FIGURE 4: Effects of ligand-mimetic peptides on αIIbβ3 molecular weight distribution determined by sedimentation equilibrium measurements. Sedimentation equilibrium profiles for αIIbβ3 alone (open circles) and in the presence of RGDF (0.6 mM, black circles), FGDR (0.6 mM, gray circles), and RGDS (0.6 mM, gray triangles), expressed as absorbance at 280 nm vs the square of the radial distance following a 22 h equilibration period at 8000 rpm. Solid lines were obtained by fitting these (and several additional data sets) globally to a single ideal species model (using NONLIN). This procedure yielded the following M_w values: 229 ± 10 K for the αIIbβ3 complex alone, 254 ± 14 K in the presence of RGDF, and 236 ± 11 K in the presence of FDGR. Similar procedures yielded M_w = 260 ± 21 K in the presence of RGDS and 196 ± 18 K in the presence of SDGR (the latter data not shown here). Deviations between the calculated and experimental points are shown in the insert.

Effects of Transient Integrin Exposure to a Ligand-Mimetic Peptide. The effects of short-term exposure of αIIbβ3 to RGDF were examined by incubating the receptor with 0.5 mM peptide for 45 min and then separating the integrin from its low molecular weight ligand by rapid gel filtration. The effects on integrin conformation were then examined by light scattering and sedimentation velocity. As can be seen in Figure 5A, addition of RGDF increased the Stokes radius of the αIIbβ3 integrin by ~13%, whereas control peptide FDGR caused only a 2% increase. Following peptide removal, R_s decreased by ~5%, to an intermediate value between its initial and ligand-modulated value. During this same cycle, M_w (light scattering) increased from 250 ± 3 K (no ligand) to 274 ± 7 K (with RGDF) and remained at nearly the same value, 277 ± 6 K, following peptide removal.

Figure 5B shows the effects of adding/removing RGDF on the distribution of sedimenting species, determined in a series of sedimentation velocity experiments. αIIbβ3 alone exhibited a peak in the $g(s^*)$ profile at 8.7 S; this parameter shifted to 8.3 S in the presence of 0.5 mM RGDF. Following removal of RGDF, the $g(s^*)$ profile exhibited a pattern midway between its initial and ligand-altered value, with a peak now at 8.5 S. Taken together, these experiments suggest that exposure of αIIbβ3 to RGDF results in changes that are partly but incompletely reversed upon removal of excess ligand-mimetic peptide.

Effects of Ligand-Mimetic Peptides on the Appearance of αIIbβ3, As Observed by Electron Microscopy. Complexes of αIIbβ3 were diluted in 0.05 M ammonium formate buffer, pH 7.4, 30 mM octyl glucoside, and 70% glycerol to a final concentration of 20 μg/mL, sprayed onto freshly cleaved mica, and shadowed with tungsten. As can be seen in Figure 6A, these preparations had a consistent appearance of a

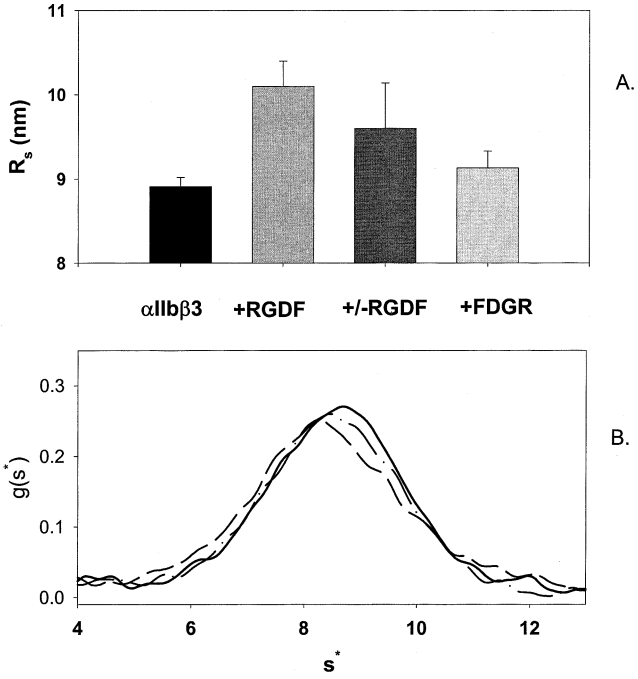

FIGURE 5: Effects of transient exposure of αIIbβ3 to a ligand-mimetic peptide. Upper panel: Changes in the αIIbβ3 Stokes radius before (black bar), during (light gray bar), and after (solid gray bar) incubation with 0.5 mM RGDF. Note how R_s increased in the presence of RGDF and then returned to an intermediate position between its initial and control peptide values (+FDGR bar) following rapid removal of unbound ligand. Dynamic light scattering analyses were performed as described in the legend to Figure 2. Lower panel: Changes in $g(s^*)$ profiles before (solid line), during (dashed line), and after (dash-dotted line) incubation with 0.5 mM RGDF. Note how the peak in the $g(s^*)$ profiles shifted toward a slower sedimenting species in the presence of RGDF and then returned to an intermediate value after peptide removal. Time-derivative analyses were performed as described in the legend to Figure 3.

globular head, about 8 × 12 nm, with two tails, about 15 nm long, projecting from one side. They appeared similar to previously published images (*17*, *59*) with one small difference: about 85% of the tails were joined together distally, while previously most were splayed.

Peptides at a final concentration of 0.5 mM were incubated with αIIbβ3 for 0.5 h prior to shadowing. After incubation with peptide, examination of the complexes by electron microscopy revealed a separation of the heads in many cases (Figure 6B). In other words, there were two, smaller separate nodules rather than a large, single, slightly elongated nodule. There were differences in the percentages of molecules with separated heads, depending on the peptide used: RGDF, 29%; RGDW, 19%; RGDS, 11%. Note that these numbers are probably underestimates for several reasons: (1) these molecular features are near the resolution of this technique, so that very good preparations were necessary to observe the separation, and it could have been missed in some cases; (2) the separation was more difficult to observe in oligomers of αIIbβ3, which were common in some of these preparations (see below); and (3) the separation might not be visible in complexes that lie on the surface with certain orientations. As a control, a 0.5 mM concentration of the reverse peptides was used. Here the images were essentially the same as the control without peptide. There were, however, some molecules in all preparations that appeared to have separated

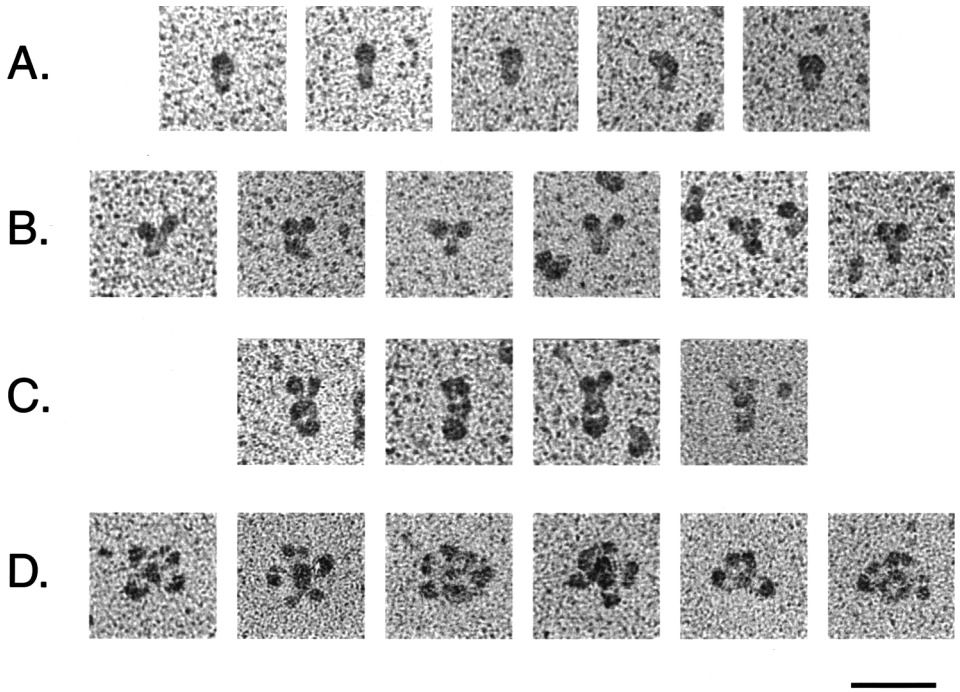

FIGURE 6: A gallery of electron microscope images of rotary-shadowed αIIbβ3 complexes with peptides. Note that these examples are of the most common types of images observed with peptide RGDF or FDGR. However, the images from other peptides are identical, although with other peptides the relative proportions of these various types of images were somewhat different, as described in detail in the text. (A) Examples of αIIbβ3 images obtained with control peptide, 0.5 mM FDGR. Each individual αIIbβ3 complex has a globular head and two long tails extending from one side. Note that most of the tails are touching each other at their ends to yield a "signet ring" shape. (B) Examples of complexes of αIIbβ3 with 0.5 mM RGDF, where there is a distinct separation between the two heads in the complexes. (C) Examples of αIIbβ3 dimers formed in the presence of 0.5 mM RGDF, in which the two complexes are joined tail to tail. There is a small nodule (or occasionally two nodules) at the tail-to-tail junction, which probably represents the detergent micelle. In many of these examples, some of the heads are separated into two nodules, as in the individual complexes in (B). (D) Examples of larger αIIBβ3 oligomers formed in 0.5 mM RGDF, in which the complexes are joined tail to tail. Under these conditions, αIIbβ3 complexes aggregate to form rosettes with their tails pointed inward and interacting and their nodular heads at the periphery. Bar = 50 nm.

heads: no peptide, 5%; FDGR, 3%; WGDR, 6%; SGDR, 8%.

Some aggregation of αIIbβ3 particles was also observed, especially in the presence of some of the peptides. Since the αIIbβ3 complexes aggregate without detergent present, 30 mM octyl glucoside was used in all experiments. Nevertheless, some aggregates were always observed, generally with tail-to-tail interactions. The amount of aggregation increased strikingly in the presence of RGDX peptides but not in the presence of reversed peptides. The percentages of total αIIbβ3 particles present in aggregates was RGDF, 66%; RGDW, 48%; RGDS, 13%; no peptide, 9%; FDGR, 8%; WGDR, 29%; and SGDR, 11%. Dimers were oriented 180° opposite each other (Figure 6C), while larger oligomers were arranged as "rosettes" (Figure 6D). In addition, there was almost invariably a small shadowed "nodule" at the tail-to-tail junction of all of these oligomers; in some cases, two such dense spots were observed. This feature of the images is likely to arise from a detergent micelle.

Given the substantial oligomerization observed by electron microscopy, selected αIIbβ3 samples were examined by light scattering in a volatile buffer, i.e., 0.05 M ammonium formate at pH 7.4 containing 30 mM octyl glucoside and 30% (v/v) glycerol. We found that αIIbβ3 alone exhibited molecular weight and Stokes radius values typical of the protomer (after correcting the data for refractive index and viscosity effects). In contrast, αIIbβ3 samples examined in 0.7 mM RGDF showed a 3-fold increase in M_w and a 4-fold increase in R_s within 30 min after peptide addition, with further increases over a 4-h period. These results indicate that oligomerization of intergrin with peptide is enhanced in the presence of glycerol. Therefore, solvent effects preclude *quantitative* comparison of electron microscopy results to those obtained by light scattering and analytical ultracentrifugation. However, *qualitative* agreement was achieved in that each technique demonstrated that RGDX peptides caused changes in the tertiary and quaternary structures of the αIIbβ3 complex. Thus, electron microscopy is useful for visualizing and interpreting the changes that are better quantified by light scattering and analytical ultracentrifugation.

Modeling the Ligand-Induced Changes in the αIIbβ3 Structure. New domain models of the αIIbβ3 complex were developed and their hydrodynamic properties computed using the BEAMS system (*36*), first to optimize the agreement between its calculated hydrodynamic parameters and those reported in this work. (Full details and stereo images of the new model are presented in the Appendix.) Here we want to point out that a small elongation of the "stalk" region yielded a new model for the ligand-free conformer (Figure 7A) that exhibited computed sedimentation ($s^0_{20,w}$) and translational diffusion ($D^0_{20,w}$) coefficients of 8.40 S and 3.11 F, respectively.

The calculated sedimentation coefficient reproduces the experimentally determined $g(s^*)$ peak for the ligand-free protomer, 8.4 ± 0.2 S. The calculated translational diffusion coefficient is approximately 7% larger than the experimental

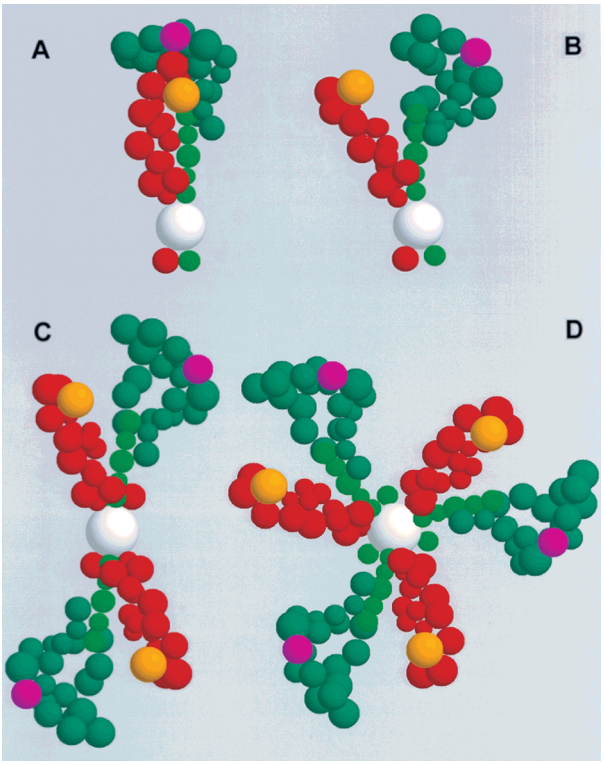

FIGURE 7: Bead models of the αIIbβ3 complex and its oligomers in the absence/presence of RGDX peptides. Panel A: bead model of the closed conformation of αIIbβ3 embedded in a single OG micelle (white bead). Panel B: the open conformer obtained upon RDGX binding. Panel C: a model for the αIIbβ3 dimer with the membrane spanning regions of both integrins embedded in a single OG micelle. Panel D: a rosette-like integrin trimer, still with all the transmembrane portions embedded into a single OG micelle. In all panels, the αIIbβ3 subunits are color-coded according to the scheme presented in Table 2: light and dark green, αIIb light and heavy subunits, respectively; red, β3 subunit; magenta, KQAGDV primary binding site on the αIIb heavy subunit; orange, RGDX primary interaction site on the β3 subunit; and white, OG micelle containing the transmembrane portions of both αIIb and β3 subunits.

value, $D^0_{20,w} = 2.92 \pm 0.16$ F. However, small quantities of oligomers could well have contributed to the observed decrease of the *z*-average diffusion coefficient (*40*).

A model for the ligand-bound or "open" conformer was next developed (Figure 7B), based on electron microscopic observations, such as those in Figure 6B, that show a partial separation of the αIIb and β3 subunits in the presence of an RGDX ligand. We also considered the hydrodynamic data and adjusted the open model to reproduce the ligand-induced shift in the $g(s^*)$ profile, a decrease of ~7% in the peak *s* value. Thus, we obtained computed sedimentation and diffusion coefficients of 7.83 S and 2.91 F, respectively, for the open form.

However, modeling the conformational change *alone* underestimates the ~15% decrease in the diffusion coefficient observed with the most effective ligand-mimetic peptide, RGDF. Since the diffusion coefficient is more sensitive to changes in both conformation and oligomerization, the effects of integrin self-association will be addressed as well.

The analytical ultracentrifugation and electron microscope observations reported here indicate that ligand binding increased αIIbβ3 oligomer formation. These rosette-like oligomers (Figure 6D) appeared joined through their carboxy-terminal "tails", i.e., regions that contain the membrane-spanning and cytoplasmic regions of the αIIb and β3 polypeptides. Electron microscopy also demonstrated that these ligand-bound conformers often exhibited a separation of the globular region into two distinct molecular entities. These observations formed the basis for the bead models of αIIbβ_3 dimers (10.8 S, 2.02 F) and trimers (14.1 S, 1.75 F) shown in Figure 7C,D. Note that these oligomers have been assembled from the open form of the protomer.

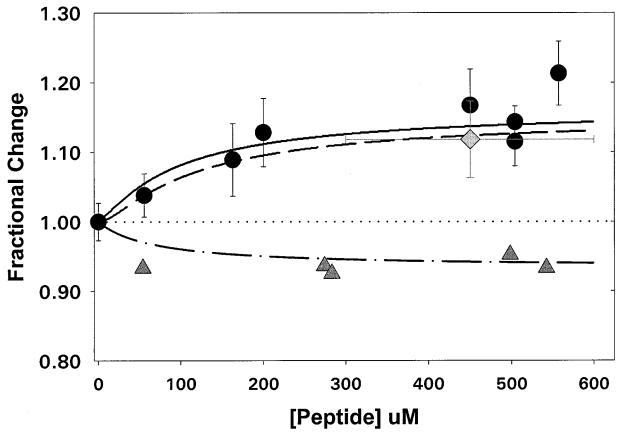

FIGURE 8: Simulations of changes in αIIbβ3's solution parameters as a function of RGDX ligand concentration. Concentrations of closed and open integrin protomers and dimers and trimers were calculated from the analytical solution to eq 1 as a function of ligand concentration. This information was combined with the modeled hydrodynamic parameters of each species to calculate the *z*-average Stokes radius, weight-average molecular weight, and peak of the sedimentation coefficient distribution. Both experimental data and simulated results are expressed as a fraction of the control value (ordinate) vs the peptide concentration (abscissa). The solid line and filled circles denote changes in the Stokes radius (R_s). The dashed line and light gray diamond denote changes in the weight-average molecular weight, M_w, obtained over the range of RGDF concentrations indicated by the bidirectional bar. The dash-dotted line and dark gray triangles denote changes in the peak of the sedimentation coefficient distribution, s_{peak}. The dotted line corresponds to no change in any parameter.

Simulations of Ligand-Induced Integrin Oligomerization. Consider a scheme in which ligand binding shifts a conformational equilibrium in favor of the open form of the αIIbβ3 integrin, followed by limited oligomerization of the ligand-bound conformers:

$$\mathrm{L} + \alpha\mathrm{IIb}\beta3 \overset{K_{conf}}{\rightleftharpoons} \alpha\mathrm{IIb}\beta3^*\cdot\mathrm{L} \overset{K_1}{\rightleftharpoons} (\alpha\mathrm{IIb}\beta3^*\cdot\mathrm{L})_2 \overset{K_1}{\rightleftharpoons} (\alpha\mathrm{IIb}\beta3^*\cdot\mathrm{L})_3 \quad (1)$$

The analytical solution of the resultant cubic equation (*60*) enables the calculation of the concentrations of each molecular species as a function of ligand concentration. Combining this information with modeled hydrodynamic parameters for each species yielded Figure 8, which is a simulation of the changes in M_w, R_s, and *s* that result from a ligand-induced oligomerization scheme. In this case, $K_{conf} = 0.015$ L/μmol^{-1} of ligand and $K_1 = 0.09$ L/μmol^{-1} of integrin; these parameters were selected empirically to optimize agreement with experiment and correspond to ~11% dimers and 1% trimers in the presence of a saturating ligand concentration. The overall agreement between the simulations and experimental data obtained with RGDF is quite satisfactory, as can be seen in Figure 8.

DISCUSSION

This study examined the molecular mechanisms that enable initially inert αIIbβ3 integrins to form activated receptors capable of binding adhesive proteins and transmitting intracellular signals (*2, 31, 61*). We have shown that the protomer, the "resting" form of αIIbβ3 isolated in octyl glucoside in the absence of ligands, behaves as an elongated heterodimeric complex whose hydrodynamic parameters and molecular morphology can be quantitatively described by a low-resolution domain map ((*34, 36*; this work).

The question remains: What molecular alterations enable αIIbβ3 to bind *macromolecular* adhesive ligands? Loftus and Liddington (*31*) proposed that, on the resting αIIbβ3 conformation, a ligand-binding segment of the β3 chain (*19, 62*) blocks another molecular recognition surface on the αIIb subunit's "propeller" fold (*8, 31, 63, 64*). The hypothesis that steric hindrance may prevent adhesive proteins from binding to αIIbβ3 is consistent with the integrin models presented in Figure 7 (and as stereo images in the Appendix). We note how, in the "closed" conformation, the I-domain-like region of the β chain (*62, 65, 66*) sits near the α subunit's putative ligand-recognition surface (*63, 64*) in a manner that could well prevent large molecules such as fibrinogen from binding.

Our data can help to explain how macromolecular ligands gain access to this buried surface and how, upon binding, a signal is transmitted through the extended transmembrane stalks to integrin's cytoplasmic domain (*8, 32, 67*). In particular, we have provided new evidence for a prompt, ligand-linked conformational change leading to an open integrin structure characterized by an increased frictional coefficient and a distinct subunit separation in the globular domain of the occupied αIIbβ3 complex.

Dynamic light scattering measurements presented here show how RGDX ligand-mimetics shifted αIIbβ3's solution conformation in a process that approached completion in minutes and was sustained for several hours. Complementary analytical ultracentrifugation data demonstrated a change in αIIbβ3's sedimentation coefficient distribution toward a slower moving form in the presence of RGDX ligands. Electron microscopy provided direct visualization of these structural alterations, in that αIIbβ3's globular domain displayed a bilobed appearance in the presence of RGDX ligands. In contrast, the control peptides of reversed sequence did not significantly affect αIIbβ3 structure.

The changes in the Stokes radius and sedimentation coefficient reported here agree with hydrodynamic calculations based on a transition from a closed to an open integrin structure. Furthermore, as can be seen in Figure 7B (and stereo models in the Appendix), the beads containing the RGD and LGGAKQAGDV cross-linking sites have shifted to new, more solvent-exposed locations in our open model. While individual domains are not discernible in our electron micrographs, we note the ~7 nm separation of the now-distinct subunits of αIIbβ3's globular domain in the presence of RGDX ligands. This gap appears well suited for docking the distal domain of the multinodular fibrinogen molecule (*17*) and is consistent with Loftus and Liddington's postulate of a ligand-induced "shape shift" to a new, high-affinity conformer where the β subunit I-domain and the α subunit propeller are separated (*31*).

We also found that the ability of RGDX ligands to perturb αIIbβ_3 conformation was influenced by the presence of a hydrophobic residue in the fourth position, in that both solution measurements and electron microscope observations generally showed more pronounced effects with RGDF and RGDW than with RGDS. This suggests that binding RGDX ligands may disrupt hydrophobic interactions that stabilize the αIIb/β3 interface in the closed integrin. These observations may help to explain earlier reports that prolonged incubation with RGDX ligands alters αIIbβ3's hydrodynamic behavior and increases its susceptibility to proteolysis (*28*) as well as why the ability of RGDX peptides to block fibrinogen binding to platelets correlates with their hydrophobicity (*68*).

In addition, we found that a slow oligomerization process follows the initial ligand-coupled isomerization of the αIIbβ3 integrin. In particular, sedimentation equilibrium measurements showed an ~10% increase in αIIbβ3's weight-average molecular weight in the presence of RGDF (at concentrations >0.2 mM). Electron microscopy also provided evidence for αIIbβ3 self-association in the presence of RGDX ligands; this oligomer-promoting ability followed the order RGDF > RGDW > RGDS. While oligomers appeared more prevalent in the electron micrographs than would be expected from the sedimentation equilibrium data, differences in sample preparation techniques probably contributed to these observations.

The oligomers we observed in the presence of ligand-mimetic peptides appeared linked through their tails. The intracellular regions of both subunits are considered to maintain the αIIbβ3 integrin in an inactive conformation, in that genetically engineered receptors lacking either the α- or β-cytoplasmic region are constitutively active (*9, 70*). Thus our observations are consistent with the postulate that conformational changes caused by receptor occupancy are transmitted from the extracellular ligand-binding domain to distal regions of the αIIbβ_3 complex, leading to clusters of activated integrins (*8, 32*). Our findings support the concept that receptor oligomerization can increase the capture efficiency of the αIIbβ3 integrin for adhesive proteins (*8, 32, 71*). This mechanism predicts that multidomainal ligands such as fibrinogen, fibrin, and von Willebrand factor (*72, 73*) can exhibit polyvalent interactions with integrin oligomers, leading to tight binding. As the signal transduction activity of many integrin receptors is thought to be regulated at least in part by self-association, it is likely that αIIbβ3 oligomerization contributes to the formation of "signaling clusters" on the surface of stimulated platelets (*8, 32, 71, 74*).

ACKNOWLEDGMENT

The expert technical assistance of Mrs. Mary Stahle is gratefully acknowledged. Sekar Nagaswami is thanked for his excellent technical skill in carrying out the electron microscopy and associated specimen preparation. Drs. J. B. Edelson and D. S. Lyles are also thanked for their critical reading of the manuscript.

APPENDIX: FEATURES OF THE REVISED αIIbβ3 MODEL

Computing Molecular Volumes. The program PROMOLP (protein molecular parameters) was used to determine the

Table 2: Sequence Assignments and Basic Properties of the αIIbβ3 Bead Model[a]

residue no.	bead no.	hydrated radius (nm)	mol wt	color	remarks
β_3 subunit					
1−62	1	1.400	6619	red	Cys5 disulfide-bonded to Cys435
63−100	2	1.371	6402	red	
101−216	3	1.774	13542	orange	RGDX primary binding site
217−298	4	1.542	8788	red	
299−365	5	1.581	9671	red	
366−389	6	0.994	2505	red	
390−402	7	0.845	1377	red	
403−422	8	0.993	2260	red	Cys406 disulfide-bonded to Cys655
423−447	9	1.034	2730	red	Cys435 disulfide-bonded to Cys5
448−498	10	1.450	7769	red	
499−537	11	1.201	4267	red	
538−578	12	1.342	6540	red	
579−633	13	1.362	5984	red	Cys614 disulfide-bonded to Cys687
634−666	14	1.074	3004	red	chain equally divided between two beads
	15	1.074	3004	red	Cys655 disulfide-bonded to Cys406
667−675	16	0.760	1077	red	
676−692	17	0.959	1884	red	Cys687 disulfide-bonded to Cys614
693−721	18	2.416	11912	white	αIIbβ3 membrane-spanning region plus octyl glucoside micelle
722−762	44	1.279	4906	red	cytoplasmic region
αIIb (light chain)					
118−137	45	1.036	2391	light green	cytoplasmic region
92−117	18	2.416	11912	white	αIIbβ3 membrane-spanning region + octyl glucoside micelle
76−91	19	0.927	1881	light green	
62−75	20	0.850	1479	light green	
46−61	21	1.156	4147	light green	
27−45	22	0.937	2176	light green	
1−26	23	1.047	2801	light green	Cys9 disulfide-bonded to Cys826 of αIIb H
αIIb (heavy chain)					
834−871	24	1.241	4429	green	
811−833	25	1.008	2550	green	Cys826 disulfide-bonded to Cys9 of αIIb L
786−810	26	1.080	3214	green	
753−785	27	1.232	4316	green	
726−752	28	1.079	2957	green	
689−725	29	1.170	3912	green	
672−688	30	1.269	5229	green	
598−671	31	1.493	7822	green	
554−597	32	1.494	8259	green	
486-553	33	1.437	7428	green	
416−485	34	1.477	8021	green	
355−415	35	1.365	6273	green	
288−354	36	1.476	7878	magenta	KQAGDV primary binding site
234−287	37	1.624	10978	green	
196−233	38	1.187	4172	green	
173−195	39	0.972	2307	green	
140−172	40	1.167	3901	green	
91−139	41	1.346	5936	green	
33−90	42	1.364	6241	green	
1−32	43	1.393	7071	green	

[a] For comparison and additional information, see Table 3 of Rocco et al. (*36*).

molecular volumes of defined polypeptide stretches from the values of each amino acid residue and carbohydrate group.[2] For the amino acids, this involved calculation of their molecular weight M_r and partial specific volume v, using data taken from Table 1 in Appendix B of McRorie and Voelker (*75*), after correcting the v values from $T = 25$ °C to $T = 20$ °C with their eq 16. Values of 99.39, 153.33, and 169.1 nm^3 were respectively employed for Man and Gal, for GlcNAc and GalNAc, and for NeuNAc (PROMOLP).

Computing Hydration. The hydration values used to compute the hydrated molecular volumes were taken from the data of Kuntz and Kauzmann (*76*). For the carbohydrate residues, values of 3 and 9 mol of H_2O/mol of residue were calculated (PROMOLP) for Man, Gal, GalNAc, and GlcNAc and for NeuNAc, respectively. A molecular volume for bound water of 24.5 Å^3, based on crystallographic data (*52*), was employed for these new models. Since this is smaller than the 30.0 Å^3 derived from water bulk properties that we used earlier, the bead radii were decreased by ∼7% overall compared to our original model (*36*).

Bead Sequence Assignments. Table 2 reports the correspondence between beads and polypeptide sequence along with the physicochemical parameters and the color code for each bead; full details of the procedures may be found in Table 3 of Rocco et al. (*36*).

Revising the αIIb Subunit Model. Changes in the αIIb moiety were mainly concentrated in the light subunit, where the stretch comprising residues 27−75 was assigned to three beads instead of one. This is a stretch where both Chou−Fasman (CF) (*77*) and Garnier−Osguthorpe−Robson (GOR) (*78*) methods predict short β-sheet regions interrupted by turns, one of which is in correspondence of an intron−exon

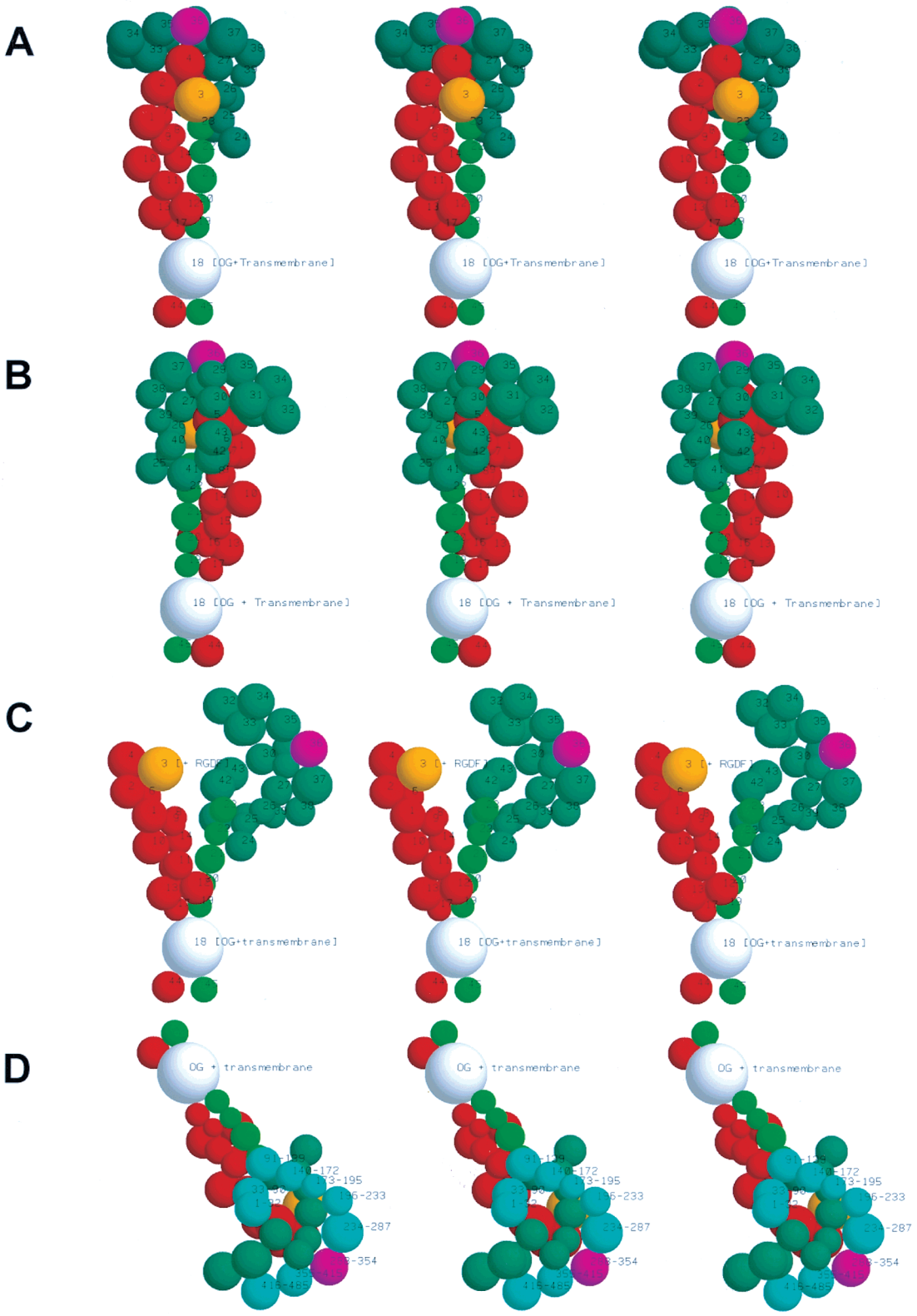

FIGURE 9: Stereoviews of the αIIbβ3 integrin models. In each panel, left and center models form a relaxed-eyes pair, while the center and right models are for crossed-eyes viewing. Panels A and B: two views from opposite sides of the revised model for αIIbβ3 in its "native", inactive conformation. Panel C: a view of the model for αIIbβ3 in its open, active conformation induced by RGDX binding. In panels A−C the beads are color-coded according to the scheme reported in Table 2: light and dark green, αIIb light and heavy subunits, respectively; red, β3 subunit; magenta, KQAGDV primary binding site on the αIIb heavy subunit; orange, RGDX primary interaction site on the β3 subunit; and white, OG micelle containing the transmembrane portions of both αIIb and β3 subunits. In panels A−C the beads are also labeled with their progressive number (see Table 2). Panel D: a view of the αIIbβ3 model where the beads corresponding to the putative β-propeller fold in the αIIb heavy subunit are highlighted in light blue (with the exception of bead 36 whose color is still magenta) and labeled with the amino acid sequences assigned to each bead. All other colors are as in panels A−C.

boundary. The new "cuts" were made roughly in correspondence with these turn zones, with one of them falling just at the intron−exon boundary. The other αIIb cut was within residues 786−833 of the stalk region of the heavy subunit, at a predicted β-sheet/turn junction (*36*, *79*).

Revising the β3 Subunit Model. First, we have split the stretch comprising residues 634−692 into four beads, instead of one. The first two beads include residues 634−666 with no further specific assignment, hence their identical radii and molecular weights (here, the chain may be thought of as going in and out of the two beads). This was done because of the internal disulfide bridge between Cys635−Cys663 (*80*) and the long-range disulfide bridge linking Cys655 to Cys406 (*80*); the end of this section corresponds to a predicted protease-sensitive turn region. Residues 667−692 were then similarly bisected at a potential turn between two short β-sheet regions that begins at residue 675.

Residues 366−402 and 423−498 were then split in two beads each. The first segment was split three residues after an internal disulfide bridge linking Cys374 to Cys386 (*80*) to maintain the connectivity between the stalk and the "head" regions. The other stretch was divided at a loop region (residues 423−447) that leads to the first clearly defined disulfide-rich unit (residues 448−498). Thus connectivity was restored, and the constraints imposed by the long-range disulfide bridge linking Cys435 to Cys5 (assigned to bead 1; see Table 1) were met.

Modeling the αIIbβ3 Protomer. The original αIIbβ3 model (*36*) was then modified by first changing all the radii values and then substituting the newly generated "multiple" beads in place of the original single ones. Since the new radii were smaller, the connectivity along the chain was then restored by sequential translations along the line connecting the centers of each bead pair, starting from the OG-transmembrane bead and keeping as much as possible the original spatial relations between the beads. Care was also taken to maintain contact between the beads containing sequence stretches linked by disulfide bridges as well as those with putative noncovalent interactions, both intra- and intersubunit (see ref *36*). The putative membrane-spanning regions of both subunits were contained within a 2.4 nm radius sphere that represents an octyl glucoside micelle, expanded from its original diameter of 2.3 nm (*34*) to accommodate the extra, unhydrated polypeptide volume.

The final result is presented in Figure 9, where in panels A and B are printed two different stereoviews, taken from opposite sides, of the revised model for αIIbβ3 (in each panel, the left and center images form a relaxed-eyes pair, while the center and right panel are for crossed-eyes view). The β3 subunit is in red, and the αIIb subunit is in two shades of green (lighter for the light subunit), while the OG micelle containing the two transmembrane portions is in white. The bead containing the main putative RDGX interaction site in the β3 subunit (*81*) is in orange, while the corresponding putative fibrinogen γ-chain interaction site in the αIIb heavy subunit (*82*) is in purple. For easy identification and cross-checking with Table 2, the beads have also been labeled with their progressive number.

In respect to our original model, this revised version is clearly more elongated, with overall dimensions now in very good agreement with those deduced from the electron micrographs. Nevertheless, the main feature of a head region superimposed over a stalk region is very similar in the two versions, with most of the changes resulting in a longer, thinner stalk. Stereoviews of the open conformer of αIIbβ3 are also reported in Figure 9C, where the magnitude of the relative shift between the two subunits can be fully appreciated.

Comparison to the Predicted "β-Propeller" Domain. One particular feature, which was already present in our original model and that is maintained in the revised version presented here, calls for further comments. In Figure 9D, a different view of the model is presented, with the beads representing the stretch between amino acids 1−485 of the αIIb heavy subunit color-coded in light blue and labeled with their sequence assignment. This region neatly encompasses the αIIb region comprising residues 1−452, which was predicted recently to fold into a β-propeller domain common to many integrin A subunits (*63*, *64*, *83*). As can be seen from the stereo image in panel D, we positioned the beads representing this region, on the basis of the biochemical evidence then available, in a circular arrangement that closely resembles the structure of the predicted β-propeller domain. No attempt was made to further improve the structural correspondence between the modeled β-propeller domain and beads' sizes and positions, due to the still speculative nature of both models, but we find the agreement between the two models to be quite striking. This result, combined with the excellent agreement between the calculated hydrodynamic properties of the revised model and the new experimental data presented here, strongly argues in favor of the new model and suggests that our low-resolution approach yields valuable structural information.

SUPPORTING INFORMATION AVAILABLE

Software that enables readers to view and manipulate the integrin models presented in this paper (Figures 7 and 9) is available free of charge via the Internet at http://pubs.acs.org.

REFERENCES

1. Schwartz, M. A., Schaller, M. D., and Ginsberg, M. H. (1995) *Annu. Rev. Cell Dev. Biol. 11*, 549−599.
2. Clark, E. A., and Brugge, J. S. (1995) *Science 268*, 233−239.
3. Hynes, R. O. (1992) *Cell 69*, 11−25.
4. Hynes, R. O. (1987) *Cell 48*, 549−554.
5. Albelda, S. M., and Buck, C. A. (1990) *FASEB J. 4*, 2868−2880.
6. Smyth, S. S., Joneckis, C. C., and Parise, L. V. (1993) *Blood 81*, 2827−2843.
7. Schwartz, M. A. (1993) *Cancer Res. 53*, 1503−1506.
8. Shattil, S. J., Kashiwagi, H., and Pampori, N. (1998) *Blood 91*, 2645−2657.
9. Stuiver, I., and O'Toole, T. E. (1995) *Stem Cells 13*, 250−262.
10. Phillips, D. R., Charo, I. F., Parise, L. V., and Fitzgerald, L. A. (1988) *Blood 71*, 831−843.
11. Plow, E. F., and Ginsberg, M. H. (1989) *Prog. Hemostasis Thromb. 9*, 117−156.
12. Fitzgerald, L. A., Steiner, B., Rall, S. C., Lo, S., and Phillips, D. R. (1987) *J. Biol. Chem. 262*, 3936−3939.
13. Lee, J.-O., Rieu, P., Arnaout, M. A., and Liddington, R. (1995) *Cell 80*, 631−638.
14. Lee, J. O., Bankston, L. A., Arnaout, M. A., and Liddington, R. C. (1995) *Structure 3*, 1333−1340.
15. Qu, A. D., and Leahy, D. J. (1996) *Structure 4*, 931−942.
16. Carrell, N. A., Fitzgerald, L. A., Steiner, B., Erickson, H. P., and Phillips, D. R. (1985) *J. Biol. Chem. 260*, 1743−1749.

17. Weisel, J. W., Nagaswami, C., Vilaire, G., and Bennett, J. S. (1992) *J. Biol. Chem. 267*, 16637−16643.
18. Nermut, M. V., Green, N. M., Eason, P., Yamada, S. S., and Yamada, K. M. (1988) *EMBO J. 7*, 4093−4099.
19. Tozer, E. C., Liddington, R. C., Sutcliffe, M. J., Smeeton, A. H., and Loftus, J. C. (1996) *J. Biol. Chem. 271*, 21978−21984.
20. Tozer, E. C., Hughes, P. E., and Loftus, J. C. (1996) *Biochem. Cell. Biol. 74*, 785−798.
21. O'Toole, T. E., Loftus, J. C., Du, X., Glass, A. A., Ruggeri, Z. M., Shattil, S. J., Plow, E. F., and Ginberg, M. H. (1990) *Cell Regul. 1*, 883−893.
22. Phillips, D. R., Charo, I. F., and Scarborough, R. M. (1991) *Cell 65*, 359−362.
23. Faull, R. J., and Ginsberg, M. H. (1995) *Stem Cells 13*, 38−46.
24. Ginsberg, M. H. (1995) *Biochem. Soc. Trans. 23*, 439−446.
25. Sims, P. J., Ginsberg, M. H., Plow, E. F., and Shattil, S. J. (1991) *J. Biol. Chem. 266*, 7345−7352.
26. Frelinger, A. L., III, Lam, S. C., Plow, E. F., Smith, M. A., Loftus, J. C., and Ginsberg, M. H. (1988) *J. Biol. Chem. 263*, 12397−12402.
27. Du, X., Plow, E. F., Frelinger, A. L., III, O'Toole, T. E., Loftus, J. C., and Ginsberg, M. H. (1991) *Cell 65*, 409−416.
28. Parise, L. V., Helgerson, S. L., Steiner, B., Nannizzi, L., and Phillips, D. R. (1987) *J. Biol. Chem. 262*, 12597−12602.
29. Mayo, K. H., Fan, F., Beavers, M. P., Eckardt, A., Keane, P., Hoekstra, W. J., and Andrade-Gordon, P. (1996) *FEBS Lett. 378*, 79−82.
30. Erb, E. M., Tangemann, K., Bohrmann, B., Müller, B., and Engel, J. (1997) *Biochemistry 36*, 7395−7402.
31. Loftus, J. C., and Liddington, R. C. (1997) *J. Clin. Invest. 100*, Suppl. 81.
32. Hughes, P. E., and Pfaff, M. (1998) *Trends Cell. Biol. 8*, 359−364.
33. Bazzoni, G., and Hemler, M. E. (1998) *Trends Biochem. Sci. 23*, 30−34.
34. Hantgan, R. R., Braaten, J. V., and Rocco, M. (1993) *Biochemistry 32*, 3935−3941.
35. Hansen, J. C., Lebowitz, J., and Demeler, B. (1994) *Biochemistry 33*, 13155−13163.
36. Rocco, M., Spotorno, B., and Hantgan, R. R. (1993) *Protein Sci. 2*, 2154−2166.
37. Ramsamooj, P., Lively, M. O., and Hantgan, R. R. (1991) *Biochem. J. 276*, 725−732.
38. Ramsamooj, P., Doellgast, G. J., and Hantgan, R. R. (1990) *Thromb. Res. 58*, 577−592.
39. Hantgan, R. R., Endenburg, S. C., Cavero, I., Marguerie, G., Uzan, A., Sixma, J. J., and De Groot, P. G. (1992) *Thromb. Haemostasis 68*, 694−700.
40. Johnson, C. S., and Gabriel, D. A. (1981) in *Spectroscopy in Biochemistry* (Bell, J. E., Ed.) Vol. II, pp 177−272, CRC Press, Boca Raton, FL.
41. Stafford, W. F., III (1992) *Anal. Biochem. 203*, 295−301.
42. Cohen, R., and Claverie, J. M. (1975) *Biopolymers 14*, 1701−1716.
43. Claverie, J. M., Dreux, H., and Cohen, R. (1975) *Biopolymers 14*, 1685−1700.
44. Philo, J. S. (1997) *Biophys. J. 72*, 435−444.
45. Johnson, M., Correia, J. J., Yphantis, D. A., and Halvorson, H. (1981) *Biophys. J. 36*, 575−588.
46. Fowler, W. E., and Erickson, H. P. (1979) *J. Mol. Biol. 134*, 241−249.
47. Weisel, J. W., Stauffacher, C. V., Bullitt, E., and Cohen, C. (1985) *Science 230*, 1388−1391.
48. Veklich, Y. I., Gorkun, O. V., Medved, L. V., Nieuwenhuizen, W., and Weisel, J. W. (1993) *J. Biol. Chem. 268*, 13577−13585.
49. Strazielle, C. (1972) in *Light Scattering from Polymer Solutions* (Huglin, M. B., Ed.) pp 633−669, Academic Press, London and New York.
50. Spotorno, B., Piccinini, L., Tassara, G., Ruggiero, C., Nardini, M., Molina, F., and Rocco, M. (1997) *Eur. Biophys. J. 25*, 373−384.
51. Denisov, V. P., Jonsson, B. H., and Halle, B. (1999) *Nat. Struct. Biol. 6*, 253−260.
52. Gerstein, M., and Chothia, C. (1996) *Proc. Natl. Acad. Sci. U.S.A. 93*, 10167−10172.
53. Sayle, R. A., and Milton, J. G. (1995) *Biochem. Sci. 20*, 374−376.
54. De La Torre, J. G., and Bloomfield, V. A. (1981) *Q. Rev. Biophys. 14*, 81−139.
55. Aerts, T., Xia, J.-Z., Slegers, H., de Block, J., and Clauwaert, J. (1990) *J. Biol. Chem. 265*, 8675−8680.
56. Eirin, M. T., Calvete, J. J., and Gonzalez-Rodriguez, J. (1986) *Biochem. J. 240*, 147−153.
57. Schubert, D., Boss, K., Dorst, H. J., Flossdorf, J., and Pappert, G. (1983) *FEBS Lett. 163*, 81−84.
58. Cantor, C. R., and Schimmel, P. R. (1980) in *Biophysical Chemistry. Part II: Techniques for the study of biological structure and function*, W. H. Freeman and Co., San Francisco, CA.
59. Carrell, N. A., Fitzgerald, L. A., Steiner, B., Erickson, H. P., and Phillips, D. R. (1985) *J. Biol. Chem. 260*, 1743−1749.
60. Beyer, W. H. (1981) in *CRC Standard Mathematical Tables*, CRC Press, Inc., Boca Raton, FL.
61. Longhurst, C. M., and Jennings, L. K. (1998) *Cell. Mol. Life Sci. 54*, 514−526.
62. Leahy, D. J. (1997) *Annu. Rev. Cell Dev. Biol. 13*, 363−393.
63. Springer, T. A. (1997) *Proc. Natl. Acad. Sci. U.S.A. 94*, 65−72.
64. Huang, C. C., and Springer, T. A. (1997) *Proc. Natl. Acad. Sci. U.S.A. 94*, 3162−3167.
65. Loftus, J. C., O'Toole, T. E., Plow, E. F., Glass, A., Frelinger, A. L., and Ginsberg, M. H. (1990) *Science 249*, 915−918.
66. Bajt, M. L., and Loftus, J. C. (1994) *J. Biol. Chem. 269*, 20913−20919.
67. Du, X., Gu, M., Weisel, J. W., Nagaswami, C., Bennett, J. S., Bowditch, R., and Ginsberg, M. H. (1993) *J. Biol. Chem. 268*, 23087−23092.
68. Tranqui, L., Andrieux, A., Hudry-Clergeon, G., Ryckewaert, J. J., Soyez, S., Chapel, A., Ginsberg, M. H., Plow, E. F., and Marguerie, G. (1989) *J. Cell Biol. 108*, 2519−2527.
69. O'Toole, T. E., Mandelman, D., Forsyth, J., Shattil, S. J., Plow, E. F., and Ginsberg, M. H. (1991) *Science 254*, 845−847.
70. O'Toole, T. E., Katagiri, Y., Faull, R. J., Peter, K., Tamura, R., Quaranta, V., Loftus, J. C., Shattil, S. J., and Ginsberg, M. H. (1994) *J. Cell Biol. 124*, 1047−1059.
71. Hato, T., Pampori, N., and Shattil, S. J. (1998) *J. Cell Biol. 141*, 1685−1695.
72. Hawiger, J. (1995) *Semin. Hematol. 32*, 99−109.
73. Hantgan, R. R., Nichols, W. L., and Ruggeri, Z. M. (1990) *Blood 75*, 889−894.
74. Simmons, S. R., Sims, P. A., and Albrecht, R. M. (1997) *Arterioscler. Thromb. Vasc. Biol. 17*, 3311−3320.
75. McRorie, D. K., and Vogel, S. N. (1993) in *Self-Associating Systems in the Analytical Ultracentrifuge*, Beckman Instruments, Inc., Palo Alto, CA.
76. Kuntz, I. D. J., and Kauzmann, W. (1974) *Adv. Protein Chem. 28*, 239−345.
77. Chou, P. Y., and Fasman, G. D. (1978) *Annu. Rev. Biochem. 47*, 251−276.
78. Garnier, J., Osguthorpe, D. J., and Robson, B. (1978) *J. Mol. Biol. 120*, 97−120.
79. Liddington, R. C., and Bankston, L. A. (1998) *Structure 6*, 937−938.
80. Calvete, J. J., Henschen, A., and González-Rodríguez, J. (1991) *Biochem. J. 274*, 63−71.
81. D'Souza, S. E., Ginsberg, M. H., Burke, T. A., Lam, S. C. T., and Plow, E. F. (1988) *Science 242*, 91−93.
82. D'Souza, S. E., Ginsberg, M. H., Burke, T. A., and Plow, E. F. (1990) *J. Biol. Chem. 265*, 3440−3446.
83. Lu, C., Oxvig, C., and Springer, T. A. (1998) *J. Biol. Chem. 273*, 15138−15147.

BI9907680